Comput. Methods Appl. Mech. Engrg. 199 (2010) 490–501

Contents lists available at ScienceDirect

Comput. Methods Appl. Mech. Engrg.

journal homepage: www.elsevier.com/locate/cma

A fast BEM for the analysis of damaged structures with bonded piezoelectric sensors

I. Benedetti [a], M.H. Aliabadi [b,*], A. Milazzo [a]

[a] DISAG – Dipartimento di Ingegneria Strutturale, Aerospaziale e Geotecnica, Universitá di Palermo, Viale delle Scienze, Edificio 8, 90128 Palermo, Italy
[b] Department of Aeronautics, Imperial College London, South Kensington Campus, London SW7 2AZ, United Kingdom

ARTICLE INFO

Article history:
Received 6 April 2009
Received in revised form 1 September 2009
Accepted 7 September 2009
Available online 21 October 2009

Keywords:
Boundary element method
Fast BEM solvers
Piezoelectric patches
SHM systems modeling

ABSTRACT

A fast boundary element method for the analysis of three-dimensional solids with cracks and adhesively bonded piezoelectric patches, used as strain sensors, is presented. The piezoelectric sensors, as well as the adhesive layer, are modeled using a 3D state-space finite element approach. The piezoelectric patch model is formulated taking into account the full electro-mechanical coupling and embodying the suitable boundary conditions and it is eventually expressed in terms of the interface variables, to allow a straightforward coupling with the underlying host structure, which is modeled through a 3D dual boundary element method, for accurate analysis of cracks. The technique is computationally enhanced, in terms of memory storage and solution time, using the hierarchical format in conjunction with a GMRES solver. An original strategy retaining the advantages of the fast hierarchical solution without increasing the implementation complexity to take into account the piezoelectric patches is proposed for the solution of the final system. The presented work is a step towards modeling of structural health monitoring systems.

1. Introduction

Structural reliability and safety are issues of critical relevance in many civil, mechanical, chemical, aeronautic and aerospace engineering applications. In recent years, structural health monitoring (SHM) has emerged as a concept in the broader field of investigation of *smart structures* [1,2]. Structural systems are usually described as *smart* when they are able to sense and adapt their response to changing operational or environmental conditions. Their development relies on the integration of sensors and actuators with the structure and on the combination with appropriate electronics, modeling and control algorithms.

SHM systems exploit such features to detect the occurrence and location of damage which may affect the performance and reliability of the structure. While conventional non-destructive inspection procedures investigate directly for damage at scheduled intervals applying the appropriate technique, *in situ* SHM systems are generally based on the real time comparison of the local or global response of the damaged structure with the known response of the undamaged one.

Structural usage and health monitoring can be accomplished by measuring, through a network of suitably arranged sensors, some physical variables and fields, such as strain, vibration, electrical conductivity and acoustic emission, which may be affected by the changes of material and geometrical conditions in proximity of the damaged area. Typical sensors for such tasks are strain gauges, accelerometers, fiber optics, piezoelectric films and piezoceramics. A brief overview of sensors and systems from the point of view of instrumentation can be found in [3].

Piezoelectric materials, in particular, are among the most widely used smart materials because of their reliability and sensitivity. By taking advantage of the direct piezoelectric effect, which refers to the generation of an electric displacement field as a consequence of a mechanical load, they are able to sense structural deformation and signal it through a variation of voltage or rate of variation of voltage [4]. The measurement of the electrical field, through the introduction of the piezoelectric coupling in the structural system, may be seen as an application of the electro-mechanical impedance method [5]. Piezoelectric sensors for SHM applications are usually employed in the form of small polyvinylidene fluoride (PVDF) patches or thin lead zirconate titanate (PZT) monolithic wafers. While PVDF elements are mainly used for sensing applications, stiffer PZT transducers can also be used for actuation purposes. They can be bonded on the surface of the structure or embedded into the structure itself and allow the determination of local values of strains. Due to their small sizes, the gradient identification for damage detection applications is often based on the use of arrays of such micro-electro-mechanical systems (MEMS).

It is then apparent from above that the design of SHM systems is a strongly multidisciplinary task involving deep understanding of structural behavior, damage mechanics, sensors characteristics,

* Corresponding author.
E-mail addresses: i.benedetti@unipa.it (I. Benedetti), m.h.aliabadi@imperial.ac.uk (M.H. Aliabadi), alberto.milazzo@unipa.it (A. Milazzo).

0045-7825/$ - see front matter © 2009 Elsevier B.V. All rights reserved.
doi:10.1016/j.cma.2009.09.007

signal processing and optimization theory. One of the key features enabling the design of such devices is the availability of reliable mathematical modeling and analysis.

Much research has been carried out about analytical and numerical modeling and simulation of smart structures and SHM systems. Many works are devoted to the modeling of single sensors and actuators. An extended bibliography about FEM and BEM modeling of sensors and actuators can be found in [6]. Zhang et al. [7] analyzed the problem of a piezoelectric layer bonded to an elastic substrate, considering the full coupling between electrical and mechanical fields. Ali et al. [8] developed an analytical model for constrained piezoelectric thin film sensors and applied the model to the analysis of the problem of detection of subsurface cracks [5]. An analytical solution for the coupled electromechanical dynamic behavior of a piezoelectric actuator bonded to an infinite orthotropic elastic medium has been developed by Huang and Sun [9]. Other works focus on the modeling of the whole SHM system, trying to take into account the various aspects comprising the damage identification strategy. Lin and Yuan [10] proposed an analytical model for an isotropic plate with integrated piezoelectric actuators and sensors for Lamb wave-based SHM systems. The detection of cracks in plates through piezo-generated Lamb waves is studied by Tua et al. [11], who considered several system parameters and proposed a methodology for locating and quantifying the extent of cracks. Fukunaga et al. [12] developed a two-stage strategy for damage identification, using a limited number of piezoelectric devices. Liu et al. [13] modeled the whole input–output behavior of composite plates with adhesively bonded piezo-sensors and actuators, using a dynamic one-dimensional piezoelectric model, thin plate orthotropic theory and multiple integral transforms. Liang and Hwu [14] focused on the online identification of holes/cracks in a structure through static-strain measures and artificial neural networks. Raghavan and Cesnik [15] proposed a generic procedure to obtain the guided waves (GWs) field excited by finite dimensions piezoelectric actuators bonded on an infinite isotropic plate. They also proposed a model for the response of piezo-sensors in GW fields, assuming them infinitely compliant. Sumant and Maiti [16] proposed a strain-based technique to detect size and location of cracks in beam-like components through discrete PZT patches and validated a BEM for such systems through the experimental results.

In this work a model for the analysis of three-dimensional damaged solids with adhesively bonded piezoelectric patches used as strain sensors is presented. The damaged structure is modeled and analyzed through a fast dual boundary element method (DBEM) based on the use of hierarchical matrices in conjunction with a GMRES iterative solver, previously developed by Benedetti et al. [17] for the analysis of large-scale cracked structures. The dual boundary element method allows to model the presence of cracks with accuracy, and its performance in terms of memory storage and solution time is improved using the hierarchical solver. The attached sensors, as well as the adhesive layer, are modeled using a 3D state-space finite element approach [18], taking into account the full electro-mechanical coupling in the piezoelectric layer. The suitable boundary conditions are embodied in the sensor model which is eventually expressed in terms of interface variables, allowing straightforward coupling with the underlying host structure. From the numerical point of view, the presence of sensors affects only some columns of the original DBEM collocation matrix, leaving the overall size of the solution system unchanged. Based on this consideration, an original strategy for the solution of the final system is proposed. Such strategy preserves the advantages related to the use of the fast hierarchical format without increasing the implementation complexity to take into account the sensors.

The paper is organized as follows. The piezoelectric patch model is first described. The basic equations of piezoelectricity are reviewed and the state-space approach is recalled. The sensor model for the considered application is then developed. In Section 3 the dual boundary element method of the host structure is briefly reviewed and the main features of the hierarchical format are revised. In Section 4 the model for the structure with attached piezoelectric patches is introduced and the strategy for the fast solution of the complete system is presented. Several numerical applications complete the work and illustrate the potential use for design of SHM systems.

2. Piezoelectric sensors modeling

In this section the model for static-strain piezoelectric sensors is described. The model is based on a generalized hybrid variational principle expressed in terms of suitable generalized variables, introduced to extend to the electro-elastic problem some techniques used in classical elasticity.

2.1. Basic equations

Let us consider a three-dimensional piezoelectric sensor with a plane mid-surface, and constant thickness h, see Fig. 1. The top and bottom surfaces are perpendicular to the poling direction x_3, while x_1x_2 is the plane of transverse isotropy. The sensor bottom surface is bounded on the surface of the host structure, through a thin adhesive layer. The elastic problem is expressed, in the chosen reference system, in terms of elastic displacements u_i, elastic strains γ_{ij} and elastic stresses σ_{ij} which have to satisfy the strain–displacement equations and the equilibrium equations

$$\gamma_{ij} = \frac{1}{2}(u_{i,j} + u_{j,i}), \quad \sigma_{ij,j} + f_i = 0, \tag{1}$$

where f_i represents the body force vector.

The electric problem, on the other hand, is described by introducing the electric potential φ, which is a scalar quantity, the electric field E_i and the electric displacement vector D_i. Such variables are linked by the following relationships:

$$E_i = -\varphi_{,i}, \quad D_{i,i} - \rho = 0, \tag{2}$$

i.e., the relationship between the electric field and potential and Gauss' law for electrostatics respectively, with ρ representing the free electric charge density.

The constitutive equations for piezoelectric materials can be expressed in tensor form as

$$\begin{aligned} \sigma_{ij} &= C_{ijkl}\gamma_{kl} - e_{ijk}E_k, \\ D_i &= e_{ikl}\gamma_{kl} + \varepsilon_{ik}E_k, \end{aligned} \tag{3}$$

where C_{ijkl} are the elastic coefficients, ε_{ij} are the dielectric constants and e_{ijk} are the piezoelectric coefficients.

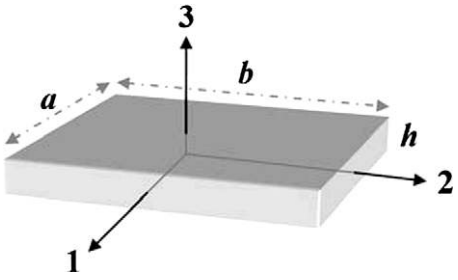

Fig. 1. Piezoelectric sensor.

Eqs. (3) can be rearranged and rewritten in matrix form as

$$\begin{bmatrix} \boldsymbol{\Sigma}_p \\ \boldsymbol{\Sigma}_z \end{bmatrix} = \begin{bmatrix} \mathbf{R}_{pp} & \mathbf{R}_{pz} \\ \mathbf{R}_{zp} & \mathbf{R}_{zz} \end{bmatrix} \begin{bmatrix} \boldsymbol{\Gamma}_p \\ \boldsymbol{\Gamma}_z \end{bmatrix}, \tag{4}$$

where $\boldsymbol{\Gamma}_p$ and $\boldsymbol{\Sigma}_p$ are generalized in-plane strains and stresses, respectively, and $\boldsymbol{\Gamma}_z$ and $\boldsymbol{\Sigma}_z$ are out-of-plane generalized strains and stresses. The exact definitions of such quantities are given in Appendix A. This representation separates the generalized in-plane quantities from the through-thickness generalized variables and it is useful for the formulation of the state-space equation of electro-elasticity.

The generalized strain–displacement relationship can be written as

$$\begin{bmatrix} \boldsymbol{\Gamma}_p \\ \boldsymbol{\Gamma}_z \end{bmatrix} = \begin{bmatrix} \mathscr{D}_\alpha \\ \mathscr{D}_\beta + \mathbf{I}\frac{\partial}{\partial x_3} \end{bmatrix} \mathbf{U}, \tag{5}$$

where $\mathbf{U} = [\,u_1 \quad u_2 \quad u_3 \quad \varphi\,]^T$ are the generalized displacements and $\mathscr{D}_\alpha$ and $\mathscr{D}_\beta$ are linear matrix differential operators whose expressions are given in Appendix A.

2.2. Elemental state-space equation

The previous definition of the generalized variables is the basis for the *state-space* formulation of the piezoelectric problem [19,20]. The state-space formulation can be deduced starting from a generalized hybrid functional [18] whose variation with respect to the generalized variables $\mathbf{U}$ and $\boldsymbol{\Sigma}_z$ gives the generalized state-space equation

$$\frac{\partial \mathbf{Y}}{\partial x_3} = \frac{\partial}{\partial x_3}\begin{bmatrix} \mathbf{U} \\ \boldsymbol{\Sigma}_z \end{bmatrix} = \begin{bmatrix} \mathscr{A}_{11} & \mathscr{A}_{12} \\ \mathscr{A}_{21} & \mathscr{A}_{22} \end{bmatrix} \begin{bmatrix} \mathbf{U} \\ \boldsymbol{\Sigma}_z \end{bmatrix} = \mathscr{A}\mathbf{Y}. \tag{6}$$

The expression of the operators $\mathscr{A}_{ij}$ appearing in the previous relationship, together with some other details about its derivation from variational principles, is given in Appendix B. The state-space representation (6), together with the corresponding boundary conditions given in Appendix, can be used for the analysis of composite laminated plates with piezoelectric layers and allows to build an analytic solution for some cases. However, to model the attached electro-elastic sensors, a suitably discretized counterpart of Eq. (6) is needed. The discretized state-space equation is obtained subdividing the sensor area in a certain number of elements and expressing the field variables for each element through appropriate shape functions $N_i(x,y)$ and nodal variables $\delta_i(z)$. In the present work eight-node quadrilateral elements are considered to interface the sensor elements with the mesh of the host structures. Elements with other shapes and a different number of nodes can however be used. Each node carries eight degrees of freedom expressing nodal generalized displacements and out-of-plane generalized stresses.

To obtain the elemental state-space equation let us introduce the following model for the state-space variables:

$$\mathbf{Y} = \begin{bmatrix} \mathbf{U} \\ \boldsymbol{\Sigma}_z \end{bmatrix} = \begin{bmatrix} \mathbf{N}(\xi,\eta) & \mathbf{0} \\ \mathbf{0} & \mathbf{N}(\xi,\eta) \end{bmatrix} \begin{bmatrix} \widetilde{\mathbf{U}}(x_3) \\ \widetilde{\boldsymbol{\Sigma}}(x_3) \end{bmatrix} = \widetilde{\mathbf{N}}(\xi,\eta)\widetilde{\mathbf{Y}}(x_3), \tag{7}$$

where

$$\begin{aligned} \widetilde{\mathbf{U}}(x_3)^T &= \begin{bmatrix} \tilde{\mathbf{u}}_1^T & \tilde{\mathbf{u}}_2^T & \tilde{\mathbf{u}}_3^T & \tilde{\boldsymbol{\varphi}}^T \end{bmatrix} = \begin{bmatrix} \tilde{\mathbf{u}}^T & \tilde{\boldsymbol{\varphi}}^T \end{bmatrix}, \\ \widetilde{\boldsymbol{\Sigma}}(x_3)^T &= \begin{bmatrix} \tilde{\boldsymbol{\sigma}}_{13}^T & \tilde{\boldsymbol{\sigma}}_{23}^T & \tilde{\boldsymbol{\sigma}}_{33}^T & \widetilde{\mathbf{D}}_3^T \end{bmatrix} = \begin{bmatrix} \tilde{\boldsymbol{\sigma}}^T & \widetilde{\mathbf{D}}^T \end{bmatrix} \end{aligned} \tag{8}$$

and $\mathbf{N}(\xi,\eta)$ is the (4×32) shape functions matrix whose explicit expression is given in Appendix A. The vector $\tilde{\mathbf{u}}_1$ in Eq. (8), for instance, contains the displacements of the element nodes along the first coordinate direction and analogous meaning with respect to the other variables have the other vectors.

Substituting Eq. (7) into the functional (B.1), varying with respect to the nodal variables $\widetilde{\mathbf{U}}$ and $\widetilde{\boldsymbol{\Sigma}}$ and applying the divergence theorem, the following equation is obtained:

$$\mathbf{P}\frac{d\widetilde{\mathbf{Y}}(x_3)}{dx_3} = \mathbf{Q}\widetilde{\mathbf{Y}}(x_3) \tag{9}$$

with

$$\mathbf{P} = \int_S \widetilde{\mathbf{N}}^T(\xi,\eta)\widetilde{\mathbf{N}}(\xi,\eta)J(\xi,\eta)\,d\xi\,d\eta \tag{10}$$

and

$$\mathbf{Q} = \int_S \begin{bmatrix} \mathbf{Q}_{11} & \mathbf{Q}_{12} \\ \mathbf{Q}_{21} & \mathbf{Q}_{22} \end{bmatrix} J(\xi,\eta)\,d\xi\,d\eta, \tag{11}$$

where $dS = J(\xi,\eta)\,d\xi\,d\eta$ denotes the elemental base area of the sensor element. The expressions of the blocks Q_{ij} are reported in Appendix A.

Eq. (9) can be integrated and the resulting expression can be written as

$$\widetilde{\mathbf{Y}}(x_3) = exp\{\mathbf{P}^{-1}\mathbf{Q}x_3\}\widetilde{\mathbf{Y}}(0) = \mathbf{L}(x_3)\widetilde{\mathbf{Y}}(0). \tag{12}$$

If the sensor is a single-layer piezoelectric element with thickness h, the previous equation can be written as

$$\begin{bmatrix} \tilde{\mathbf{u}}_2 \\ \tilde{\boldsymbol{\varphi}}_2 \\ \tilde{\boldsymbol{\sigma}}_2 \\ \widetilde{\mathbf{D}}_2 \end{bmatrix} = \begin{bmatrix} \mathbf{L}_{uu}(h) & \mathbf{L}_{u\varphi}(h) & \mathbf{L}_{u\sigma}(h) & \mathbf{L}_{ud}(h) \\ \mathbf{L}_{\varphi u}(h) & \mathbf{L}_{\varphi\varphi}(h) & \mathbf{L}_{\varphi\sigma}(h) & \mathbf{L}_{\varphi d}(h) \\ \mathbf{L}_{\sigma u}(h) & \mathbf{L}_{\sigma\varphi}(h) & \mathbf{L}_{\sigma\sigma}(h) & \mathbf{L}_{\sigma d}(h) \\ \mathbf{L}_{du}(h) & \mathbf{L}_{d\varphi}(h) & \mathbf{L}_{d\sigma}(h) & \mathbf{L}_{dd}(h) \end{bmatrix} \begin{bmatrix} \tilde{\mathbf{u}}_1 \\ \tilde{\boldsymbol{\varphi}}_1 \\ \tilde{\boldsymbol{\sigma}}_1 \\ \widetilde{\mathbf{D}}_1 \end{bmatrix}, \tag{13}$$

where, to simplify the notation, quantities relative to h_i have been denoted by the subscript i.

Once Eq. (13) has been set, the model for the piezoelectric sensor is obtained by applying suitable bottom and top electrical and mechanical boundary conditions.

2.3. Sensor model

Let us consider the scheme reported in Fig. 2, representing a piezoelectric sensor attached on a host structure. To model the response of such system it is necessary to interface the sensor model with the host structure model. The strategy adopted in the present work is described in the following.

Piezoelectric transducers are usually made of thin sheets of piezoelectric ceramic with top and bottom surfaces covered with a conductive film serving as an electrode. The top and bottom surfaces are then equipotential and it is possible to assume without loss of generality that $\tilde{\boldsymbol{\varphi}}_1 = \mathbf{0}$ and $\tilde{\varphi}_{2,i} = \phi = cost\ \forall i$. It is worth noting that the last condition may be written as

$$\tilde{\varphi}_{2,i} - \tilde{\varphi}_{2,1} = 0, \quad i = 2,\ldots,8 \tag{14}$$

or, in matrix form as

$$\mathbf{B}\tilde{\boldsymbol{\varphi}}_2 = \mathbf{0}, \tag{15}$$

where $\mathbf{B}$ is a (7×8) matrix.

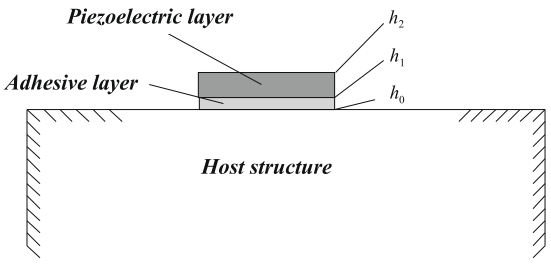

Fig. 2. Piezoelectric sensor bonded on the host structure.

Moreover, applying open-circuit boundary conditions, a complementary equation is given by

$$Q_{top} = \int_{A_t} D_3 \, dA = 0, \tag{16}$$

which expresses the conservation of the free electric charge on the sensor top surface. Expressing the electric displacement by means of shape functions and nodal values, it is possible to write

$$Q_{top} = \int_{A_t} \mathbf{N}_s(\xi,\eta) J(\xi,\eta) \widetilde{\mathbf{D}}_2 \, d\xi \, d\eta = \mathbf{b}^T \widetilde{\mathbf{D}}_2 = 0, \tag{17}$$

where $\mathbf{b}^T$ is the (1×8) row vector obtained by integrating over the sensor face the product between the shape functions vector and the Jacobian.

It is to be noted that, following the introduced notation, the symbol $\widetilde{\mathbf{D}}_2$ used in the previous equations collects the nodal values of the component D_3 of the electric displacement at the top surface. It is then a vector of nodal values, and it must not be confused with the component D_2 of the electric displacement, that does not enter the formulation.

The mechanical boundary conditions can be obtained by considering that the sensor is bonded on the surface of the host structure. Its top surface is then stress free and then

$$\tilde{\boldsymbol{\sigma}}_2 = \mathbf{0}. \tag{18}$$

Note that the previous equation, always following the introduced notation, expresses the following conditions:

$$\tilde{\boldsymbol{\sigma}}_2 = \tilde{\boldsymbol{\sigma}}(h_2) = \begin{bmatrix} \tilde{\sigma}_{13}(h_2) \\ \tilde{\sigma}_{23}(h_2) \\ \tilde{\sigma}_{33}(h_2) \end{bmatrix} = \mathbf{0}. \tag{19}$$

Using the equipotentiality condition at the bottom face $\tilde{\boldsymbol{\varphi}}_1 = \mathbf{0}$ and the mechanical condition on the top face (19), the following equations can be written:

$$\mathbf{L}_{\varphi u}\tilde{\mathbf{u}}_1 + \mathbf{L}_{\varphi\sigma}\tilde{\boldsymbol{\sigma}}_1 + \mathbf{L}_{\varphi d}\widetilde{\mathbf{D}}_1 = \tilde{\boldsymbol{\varphi}}_2, \tag{20}$$

$$\mathbf{L}_{\sigma u}\tilde{\mathbf{u}}_1 + \mathbf{L}_{\sigma\sigma}\tilde{\boldsymbol{\sigma}}_1 + \mathbf{L}_{\sigma d}\widetilde{\mathbf{D}}_1 = \mathbf{0}, \tag{21}$$

$$\mathbf{L}_{du}\tilde{\mathbf{u}}_1 + \mathbf{L}_{d\sigma}\tilde{\boldsymbol{\sigma}}_1 + \mathbf{L}_{dd}\widetilde{\mathbf{D}}_1 = \widetilde{\mathbf{D}}_2. \tag{22}$$

The equipotentiality at the top face is enforced by pre-multiplying Eq. (20) by $\mathbf{B}$. The condition (17) is enforced by pre-multiplying Eq. (22) by $\mathbf{b}^T$. The following equations are thus obtained:

$$\mathbf{B}(\mathbf{L}_{\varphi u}\tilde{\mathbf{u}}_1 + \mathbf{L}_{\varphi\sigma}\tilde{\boldsymbol{\sigma}}_1 + \mathbf{L}_{\varphi d}\widetilde{\mathbf{D}}_1) = \mathbf{0}, \tag{23}$$

$$\mathbf{b}^T(\mathbf{L}_{du}\tilde{\mathbf{u}}_1 + \mathbf{L}_{d\sigma}\tilde{\boldsymbol{\sigma}}_1 + \mathbf{L}_{dd}\widetilde{\mathbf{D}}_1) = 0. \tag{24}$$

Such conditions allow to express the vector $\widetilde{\mathbf{D}}_1$ as a function of $\tilde{\mathbf{u}}_1$ and $\tilde{\boldsymbol{\sigma}}_1$, i.e. the mechanical variables at the bottom surface of the piezoelectric patch.

Writing

$$\widetilde{\mathbf{D}}_1 = \widehat{\mathbf{L}}_{du}\tilde{\mathbf{u}}_1 + \widehat{\mathbf{L}}_{d\sigma}\tilde{\boldsymbol{\sigma}}_1, \tag{25}$$

where $\widehat{\mathbf{L}}_{du}$ and $\widehat{\mathbf{L}}_{d\sigma}$ are obtained by Eqs. (23) and (24), and substituting in Eqs. (20) and (21) one gets

$$\widehat{\mathbf{L}}_{\sigma u}\tilde{\mathbf{u}}_1 + \widehat{\mathbf{L}}_{\sigma\sigma}\tilde{\boldsymbol{\sigma}}_1 = \mathbf{0}, \tag{26}$$

$$\widehat{\mathbf{L}}_{\varphi u}\tilde{\mathbf{u}}_1 + \widehat{\mathbf{L}}_{\varphi\sigma}\tilde{\boldsymbol{\sigma}}_1 = \tilde{\boldsymbol{\varphi}}_2 \tag{27}$$

with

$$\widehat{\mathbf{L}}_{\sigma u} = \mathbf{L}_{\sigma u} + \mathbf{L}_{\sigma d}\widehat{\mathbf{L}}_{du}; \quad \widehat{\mathbf{L}}_{\sigma\sigma} = \mathbf{L}_{\sigma\sigma} + \mathbf{L}_{\sigma d}\widehat{\mathbf{L}}_{d\sigma}, \tag{28}$$

$$\widehat{\mathbf{L}}_{\varphi u} = \mathbf{L}_{\varphi u} + \mathbf{L}_{\varphi d}\widehat{\mathbf{L}}_{du}; \quad \widehat{\mathbf{L}}_{\varphi\sigma} = \mathbf{L}_{\varphi\sigma} + \mathbf{L}_{\varphi d}\widehat{\mathbf{L}}_{d\sigma}. \tag{29}$$

If an adhesive layer with thickness d is considered, an equation analogous to Eq. (13) can be written as

$$\begin{bmatrix} \tilde{\mathbf{u}}_1 \\ \tilde{\boldsymbol{\sigma}}_1 \end{bmatrix} = \begin{bmatrix} \mathbf{A}_{uu}(d) & \mathbf{A}_{u\sigma}(d) \\ \mathbf{A}_{\sigma u}(d) & \mathbf{A}_{\sigma\sigma}(d) \end{bmatrix} \begin{bmatrix} \tilde{\mathbf{u}}_0 \\ \tilde{\boldsymbol{\sigma}}_0 \end{bmatrix}. \tag{30}$$

Such equation can be obtained by writing the purely mechanical version of the elemental state-space equation (9) for the adhesive layer, and then integrating between h_0 and h_1. The subscripts 0 and 1 in Eq. (30) refer to h_0 and h_1. Using the continuity conditions at the interface between the bottom surface of the sensor and the top surface of the adhesive layer, from Eqs. (26), (27) and (30) one gets

$$\mathbf{S}_{\sigma u}\tilde{\mathbf{u}}_0 + \mathbf{S}_{\sigma\sigma}\tilde{\boldsymbol{\sigma}}_0 = \mathbf{0}, \tag{31}$$

$$\mathbf{S}_{\varphi u}\tilde{\mathbf{u}}_0 + \mathbf{S}_{\varphi\sigma}\tilde{\boldsymbol{\sigma}}_0 = \tilde{\boldsymbol{\varphi}}_2 \tag{32}$$

with

$$\mathbf{S}_{\sigma u} = \widehat{\mathbf{L}}_{\sigma u}\mathbf{A}_{uu} + \widehat{\mathbf{L}}_{\sigma\sigma}\mathbf{A}_{\sigma u}; \quad \mathbf{S}_{\sigma\sigma} = \widehat{\mathbf{L}}_{\sigma u}\mathbf{A}_{u\sigma} + \widehat{\mathbf{L}}_{\sigma\sigma}\mathbf{A}_{\sigma\sigma}, \tag{33}$$

$$\mathbf{S}_{\varphi u} = \widehat{\mathbf{L}}_{\varphi u}\mathbf{A}_{uu} + \widehat{\mathbf{L}}_{\varphi\sigma}\mathbf{A}_{\sigma u}; \quad \mathbf{S}_{\varphi\sigma} = \widehat{\mathbf{L}}_{\varphi u}\mathbf{A}_{u\sigma} + \widehat{\mathbf{L}}_{\varphi\sigma}\mathbf{A}_{\sigma\sigma}. \tag{34}$$

Eqs. (31) and (32) can be further manipulated to give

$$\tilde{\boldsymbol{\sigma}}_0 = -\mathbf{S}_{\sigma\sigma}^{-1}\mathbf{S}_{\sigma u}\tilde{\mathbf{u}}_0, \tag{35}$$

$$\tilde{\boldsymbol{\varphi}}_2 = (\mathbf{S}_{\varphi u} - \mathbf{S}_{\varphi\sigma}\mathbf{S}_{\sigma\sigma}^{-1}\mathbf{S}_{\sigma u})\tilde{\mathbf{u}}_0. \tag{36}$$

Eq. (35) coupled with the boundary element method of the host structure allows the computation of the unknowns $\tilde{\mathbf{u}}_0$. Once their values are known, Eq. (36) can be used for computing the sensor top surface electric potential $\tilde{\boldsymbol{\varphi}}_2$.

However, before coupling Eq. (35) with the 3D boundary element method of the host structure, some further consideration must be done. First, the components of the vector $\tilde{\boldsymbol{\sigma}}_0$ are stresses, not tractions, and it is then necessary to take it into account. Moreover, the sensor equations have been written with respect to a local reference system and it is then necessary to transform them according to a suitable law to get the equations in the global or host structure reference systems. Once such operations have been performed for the single sensor element it is possible to write

$$\mathbf{t}_0^h = \boldsymbol{\Psi}\mathbf{u}_0^h; \quad \boldsymbol{\varphi}_2 = \boldsymbol{\Phi}\mathbf{u}_0^h \tag{37}$$

with

$$\boldsymbol{\Psi} = \boldsymbol{\Lambda}^{-1}\mathbf{S}_{\sigma\sigma}^{-1}\mathbf{S}_{\sigma u}\boldsymbol{\Lambda}; \quad \boldsymbol{\Phi} = (\mathbf{S}_{\varphi u} - \mathbf{S}_{\varphi\sigma}\mathbf{S}_{\sigma\sigma}^{-1}\mathbf{S}_{\sigma u})\boldsymbol{\Lambda}, \tag{38}$$

where $\boldsymbol{\Lambda}$ is the rotation matrix and $\mathbf{u}_0^h$ and $\mathbf{t}_0^h$ are nodal displacements and tractions in the host structure reference system.

3. Dual boundary element method of the host structure

In the previous section the sensor model was expressed in terms of displacements and tractions at the interface with the host structure. Such quantities are unknown and their determination requires the solution of the damaged structure/bonded sensors system. It is then necessary to couple the sensor equations with the host structure model. In the present work, the host structure is modeled using the dual boundary element method.

The dual boundary element method is a general and efficient technique for modeling both two-dimensional [21,22] and three-dimensional [23,24] crack problems in the framework of the BEMs [25,26]. The method is based on the use of two independent boundary integral equations, namely the displacement integral equations, collocated on the external boundary and on one of the crack surfaces, and the traction integral equations, collocated on the other crack surface and introduced to overcome the problems originating from the coincidence of the crack nodes.

Assuming continuity of displacements at the boundary nodes, the boundary integral representation for the displacements u_j is given by

$$c_{ij}(\boldsymbol{x}_0)u_j(\boldsymbol{x}_0) + \oint_\Gamma T_{ij}(\boldsymbol{x}_0,\boldsymbol{x})u_j(\boldsymbol{x})\,d\Gamma = \int_\Gamma U_{ij}(\boldsymbol{x}_0,\boldsymbol{x})t_j(\boldsymbol{x})\,d\Gamma, \tag{39}$$

where U_{ij} and T_{ij} represent the Kelvin displacement and traction fundamental solutions at the boundary point $\boldsymbol{x}$ when collocating at the point $\boldsymbol{x}_0$, c_{ij} are coefficients depending on the boundary geometry and computed through rigid body considerations and the symbol $\oint$ stands for Cauchy principal value integral, whose presence is a consequence of the $O(r^{-2})$ strength of the T_{ij} integrands.

The displacement equation (39) is collocated on the boundary Γ and on one of the crack surfaces. When collocated at the crack node $\boldsymbol{x}_0^-$, it assumes the form

$$c_{ij}(\boldsymbol{x}_0^-)u_j(\boldsymbol{x}_0^-) + c_{ij}(\boldsymbol{x}_0^+)u_j(\boldsymbol{x}_0^+) + \oint_\Gamma T_{ij}(\boldsymbol{x}_0^-,\boldsymbol{x})u_j(\boldsymbol{x})\,d\Gamma = \int_\Gamma U_{ij}(\boldsymbol{x}_0^-,\boldsymbol{x})t_j(\boldsymbol{x})\,d\Gamma, \tag{40}$$

where $\boldsymbol{x}_0^-$ and $\boldsymbol{x}_0^+$ are the two coincident crack nodes. For smooth crack surfaces at the point $\boldsymbol{x}_0^-$, it is $c_{ij}(\boldsymbol{x}_0^-) = c_{ij}(\boldsymbol{x}_0^+) = (1/2)\delta_{ij}$.

The traction integral equation collocated at the point $\boldsymbol{x}_0^+$, where continuity of strains is assumed, is given by

$$c_{ij}(\boldsymbol{x}_0^+)t_j(\boldsymbol{x}_0^+) - c_{ij}(\boldsymbol{x}_0^-)t_j(\boldsymbol{x}_0^-) + n_j(\boldsymbol{x}_0^+)\,{=\!\!\!\!\!\!\int}_\Gamma T_{ijk}(\boldsymbol{x}_0^+,\boldsymbol{x})u_k(\boldsymbol{x})d\Gamma = n_j(\boldsymbol{x}_0^+)\,{=\!\!\!\!\!\!\int}_\Gamma U_{ijk}(\boldsymbol{x}_0^+,\boldsymbol{x})t_k(\boldsymbol{x})\,d\Gamma, \tag{41}$$

where the kernels U_{ijk} and T_{ijk} contain derivatives of U_{ij} and T_{ij}, respectively, n_j are the components of the outward normal at the point $\boldsymbol{x}_0^+$ and ${=\!\!\!\!\!\!\int}$ stands for Hadamard principal value integral, originating from the presence of the $O(r^{-3})$ kernel T_{ijk}.

Eqs. (39)–(41) provide the boundary integral model for the analysis of general crack problems. The discrete model is built on them starting from a suitable discretization of the external boundary and the crack surfaces into a set of boundary elements over which the displacements and the tractions, as well as the geometry, are expressed by means of suitable shape functions and nodal values [26].

Care must be taken in the choice of suitable boundary elements, in order to fulfill the conditions for the existence of the singular integrals. In particular the existence of Cauchy and Hadamard principal values requires Hölder continuity of the displacements and their derivatives at the collocation points. Such restrictions can be satisfied through the use of special boundary elements. In this work the same modeling strategy as that adopted by Mi and Aliabadi [23,24] is used. The continuity of the displacement derivatives, which is the stronger constraint required for the existence of the integrals in the traction equation, is guaranteed by using *discontinuous* eight-node quadratic elements for the modeling of *both* the crack surfaces. The boundary, on which only the displacement equation is collocated, is modeled by using *continuous* eight-node quadratic elements. Further information on slightly different discretization procedures can be found in [27,28].

The DBEM leads to a linear system of the form

$$\boldsymbol{A}\boldsymbol{x} = \boldsymbol{y}, \tag{42}$$

where $\boldsymbol{x}$ is the vector of unknowns and the right-hand side $\boldsymbol{y}$ stems from the application of the boundary conditions. The collocation matrix $\boldsymbol{A}$ contains the influence coefficients and has some interesting features that must be taken into account for the development of fast solvers based on the use of the hierarchical representation [17].

3.1. Fast solution of large DBEM system

When computations involve large systems, memory storage and time requirements, besides solution accuracy, become key elements for the choice of the numerical technique to be employed. In this context, the use of hierarchical matrices [29–31] for the representation of BEM systems of equations, in conjunction with Krylov subspace methods [32–35], constitutes a recent and interesting development. Such a technique allows to speed up the computation maintaining the required accuracy and saving the storage memory needed for the collocation matrix treatment.

The hierarchical representation of boundary element matrices is based on a previous subdivision of the collocation matrix into a collection of blocks, some of which, called *low rank blocks*, admit a special compressed representation, while others, said *full rank blocks* are represented entirely. Such subdivision and the subsequent classification is built starting from the boundary element mesh and is based on the grouping of the discretization nodes and elements into clusters of close nodes and elements. A block populated by integrating over a cluster of elements whose distance, suitably defined, from the cluster of collocation nodes is above a certain threshold is called *admissible* and it can be represented in low rank format. The remaining blocks are generated and stored entirely. Low rank blocks constitute an approximation of suitably selected blocks of the discrete integral operator based, from the analytical point of view, on a suitable expansion of the kernel of the continuous integral operator [36–39]. This expansion, and consequently the existence of low rank *approximants*, is based on the *asymptotic smoothness* of the kernel functions [40], i.e. on the fact that the kernels $U_{ij}(\boldsymbol{x}_0,\boldsymbol{x})$ and $T_{ij}(\boldsymbol{x}_0,\boldsymbol{x})$ are singular only when $\boldsymbol{x}_0 = \boldsymbol{x}$. Asymptotic smoothness represents a sufficient condition for the existence of low rank approximants and it does not exclude strongly or hyper-singular kernels, such as $U_{ijk}(\boldsymbol{x}_0,\boldsymbol{x})$ and $T_{ijk}(\boldsymbol{x}_0,\boldsymbol{x})$. Moreover, the regularity of the boundary over which the approximation is carried out is not requested.

The low rank blocks are built by computing and storing only *some* of the entries of the original blocks. Such entries are computed through suitable algorithms, known as adaptive cross approximation (ACA) [38,39], that allow to reach the selected accuracy in terms of Frobenius norm.

Once the hierarchical representation of the collocation matrix has been built, the solution of the system can be conveniently computed through iterative solvers with or without preconditioners. When the condition number is high and slows down the convergence rate, as is often the case when dealing with BEM systems, a preconditioner can be computed taking full advantage of the representation in the hierarchical format. If $\mathbf{Ax} = \mathbf{y}$ is the system to be solved, then a left preconditioner is an easily invertible matrix $\mathbf{P}$ such that the condition number of the system $\mathbf{P}^{-1}\mathbf{Ax} = \mathbf{P}^{-1}\mathbf{y}$ results lower than the original one, improving thus the convergence rate of the iterative solver.

In the present work a GMRES iterative solver [41] with a preconditioner is used for the solution of the system of equations. The hierarchical representation offers the opportunity of naturally building an effective preconditioner [42,43]. A *coarse* preconditioner can be obtained by first generating a coarse approximation $\mathcal{A}(\varepsilon_p)$ of the original collocation matrix $\mathcal{A}(\varepsilon_c)$, where the relationship $\varepsilon_p > \varepsilon_c$ holds, ε denoting the selected accuracy for the hierarchical representation. This coarse approximation, with reduced memory storage, can then be decomposed through the hierarchical LU decomposition to give the preconditioner P. The resulting system

$$(\mathcal{L}\mathcal{U})^{-1}\mathcal{A}\boldsymbol{x} = (\mathcal{L}\mathcal{U})^{-1}\boldsymbol{y} \tag{43}$$

has a lower condition number and the convergence rate of iterative solvers is noticeably improved. Manipulations of the system require the use of a suitably defined arithmetic able to deal with matrices in hierarchical form [29–31].

4. Analysis of damaged structures with bonded piezoelectric sensors

The presence of sensors attached on the host structure affects the system (42) and their presences must be suitably addressed. When integrating over the boundary of the host structure, considering that at the interface between the structure itself and the attached sensors both displacements and tractions can be simultaneously different from zero, the following equation is obtained:

$$\mathbf{H}\mathbf{u} + \sum_k \widetilde{\mathbf{H}}_k \tilde{\mathbf{u}}_k^h = \mathbf{G}\mathbf{t} + \sum_k \widetilde{\mathbf{G}}_k \tilde{\mathbf{t}}_k^h, \tag{44}$$

where nodal displacements and tractions have been partitioned into two sets, depending on whether they refer to nodes belonging to the interface with the sensors, $\tilde{\mathbf{u}}$ and $\tilde{\mathbf{t}}$, or to the remaining surfaces, $\mathbf{u}$ and $\mathbf{t}$. More precisely $\tilde{\mathbf{u}}_k^h$ and $\tilde{\mathbf{t}}_k^h$ denote displacements and tractions at the nodes of the host structures belonging to the interface with the kth piezoelectric sensor. Continuity conditions require

$$\begin{aligned} \tilde{\mathbf{u}}_k^s &= \tilde{\mathbf{u}}_k^h, \\ \tilde{\mathbf{t}}_k^s &= -\tilde{\mathbf{t}}_k^h, \end{aligned} \tag{45}$$

where the superscript s refers to nodes belonging to sensors. Using such conditions and Eqs. (37a) and (44) it is then possible to write

$$\mathbf{H}\mathbf{u} + \sum_k (\widetilde{\mathbf{H}}_k + \widetilde{\mathbf{G}}_k \boldsymbol{\Psi}_k)\tilde{\mathbf{u}}_k^h = \mathbf{G}\mathbf{t}. \tag{46}$$

In the previous equation, the other boundary conditions have not yet been applied. After completing the application of the boundary conditions, the previous system assumes the form

$$\widetilde{\boldsymbol{A}}\boldsymbol{x} + \sum_k (\widetilde{\mathbf{H}}_k + \widetilde{\mathbf{G}}_k \boldsymbol{\Psi}_k)\tilde{\mathbf{u}}_k^h = \boldsymbol{y}, \tag{47}$$

which represents the BEM–FEM for the structure with bonded piezoelectric sensors. It is to be noted that the matrix $\widetilde{\boldsymbol{A}}$ is not the same as the matrix $\boldsymbol{A}$ of the original structure. However Eq. (47) can also be rewritten:

$$\boldsymbol{A}\boldsymbol{x} + \sum_k \widetilde{\mathbf{G}}_k \boldsymbol{\Psi}_k \tilde{\mathbf{u}}_k^h = \boldsymbol{y}, \tag{48}$$

where the original collocation matrix appears and where it is apparent that the presence of the piezoelectric patches affects such matrix only through the terms $\widetilde{\mathbf{G}}_k\boldsymbol{\Psi}_k$, which modify only some bands of the original collocation matrix itself. Eq. (48) can be also expressed as

$$\boldsymbol{A}\boldsymbol{x} + \boldsymbol{\Phi}_{pz}\boldsymbol{x}_{pz} = \boldsymbol{y}. \tag{49}$$

The vector $\boldsymbol{x}_{pz}$ collects all the unknown displacements that multiply the columns belonging to the matrix $\boldsymbol{\Phi}_{pz}$ introduced by the presence of the sensors. It is worth noting that the vector $\boldsymbol{x}$ itself can be rearranged in two parts, one of which is $\boldsymbol{x}_{pz}$. The form of Eq. (49) is particularly appropriate to be used for the iterative solution of the system. Once the displacements are obtained from the solution of Eq. (49), Eq. (37) allows the determination of the electric potential $_k$.

4.1. Fast iterative system solution

As seen in the previous sections, a fast solution of DBEM systems of equations can be obtained by using Krylov iterative solvers in conjunction with a hierarchical representation of the collocation matrix.

The BEM analysis of the damaged structures with attached piezoelectric sensors can be carried out by using Eq. (49), where the terms $\boldsymbol{\Phi}_{pz}\boldsymbol{x}_{pz}$ are due to the presence of the sensors. The form of such equation is particularly advantageous for the hierarchical-iterative solution of the problem. In the present model, a single sensor modeled with an eight-node element modifies 24 columns of the original collocation matrix. Since it can be reasonably assumed that the number of elements related to piezoelectric sensors is considerably less than the total number of boundary elements, the fast hierarchical DBEM can be employed as follows.

The hierarchical counterpart of Eq. (49) is

$$\mathcal{A}\boldsymbol{x} + \boldsymbol{\Phi}_{pz}\boldsymbol{x}_{pz} = \boldsymbol{y}, \tag{50}$$

where $\mathcal{A}$ is the collocation matrix of the damaged structure without sensors expressed in hierarchical format, $\boldsymbol{\Phi}_{pz}$ is the matrix, expressed in full format, collecting the contributions related to the sensors and $\boldsymbol{x}_{pz}$ is a suitably rearranged subset of the vector of unknowns $\boldsymbol{x}$, collecting the components of displacements of the nodes at the interface between the host structure and the sensors. Since the matrix in full format $\boldsymbol{\Phi}_{pz}$ contains a number of columns considerably less than that of the original collocation matrix, its presence does not affect significantly the performance of the GMRES solver. In the present work, to accelerate the convergence of the iterative solver, a hierarchical LU preconditioner is used. The GMRES is then used for the rapid solution of the following system:

$$(\mathcal{L}\mathcal{U})^{-1}(\mathcal{A}\boldsymbol{x} + \boldsymbol{\Phi}_{pz}\boldsymbol{x}_{pz}) = (\mathcal{L}\mathcal{U})^{-1}\boldsymbol{y}, \tag{51}$$

where $(\mathcal{L}\mathcal{U})$ is a coarse hierarchical LU decomposition of $\mathcal{A}$.

It is worth noting that since the presence of the sensors does not affect considerably the response of the structure, $(\mathcal{L}\mathcal{U})$ is close to the LU decomposition of the matrix of the whole structure, i.e. of the matrix of the damaged structure including the bonded sensors.

The proposed solution strategy allows to analyze the structure with bonded sensors using the fast numerical scheme developed in [17], without reducing the performances of the fast hierarchical GMRES.

5. Numerical results

In this section the results of some numerical experiments, performed using the above-mentioned BEM approach, are reported.

First, the sensor numerical model is validated against a simple benchmark. An isolated sensor with electrode surfaces is considered and the *output voltage* following the application of prescribed strains *at the base* of the piezoelectric patch is measured. Strains are imposed through prescribed displacements at the base of the sensor, such variables being the quantities directly entering the model. The output is compared with the results of some simplified analytical model, as the one used for example by Lin and Yuan [10], which showed good agreement with the experimental results. Such model predicts

$$V_{out} = \frac{d_{31}E_p h_p \gamma_p}{k_{33}(1-\nu_p)}, \tag{52}$$

where $E_p = C_{11} = C_{22}$ and ν_p are the in-plane Young's modulus and Poisson's ratio of the piezoelectric material, h_p is the thickness of the piezoelectric patch, k_{33} is the dielectric permittivity along the thickness direction and d_{31} is the piezoelectric constant relating γ_{11} to E_3 or D_3 to σ_{11} in the constitutive equations

$$\begin{bmatrix} \boldsymbol{\gamma} \\ \mathbf{D} \end{bmatrix} = \begin{bmatrix} \mathbf{S} & \mathbf{d}^T \\ \mathbf{d} & \boldsymbol{\varepsilon} \end{bmatrix} \begin{bmatrix} \boldsymbol{\sigma} \\ \mathbf{E} \end{bmatrix} \tag{53}$$

and whose value can be easily obtained by manipulating Eqs. (3). γ_p is the value of the strain at the center of the piezoelectric patch, assumed constant over all the sensor in the simplified analytical model, due to the small sensor size.

Table 1
Material constants for PZT4.

	C_{11}	C_{22}	C_{33}	C_{12}	C_{13}	C_{23}	C_{44}	C_{55}	C_{66}
GPa	139	139	115	77.80	74.30	74.30	25.60	25.60	30.60
	e_{31}	e_{32}	e_{33}	e_{24}	e_{15}				
C/m^2	−5.20	−5.20	15.08	12.72	12.72				
	k_{11}	k_{22}	k_{33}						
nFa/m	13.06	13.06	11.51						

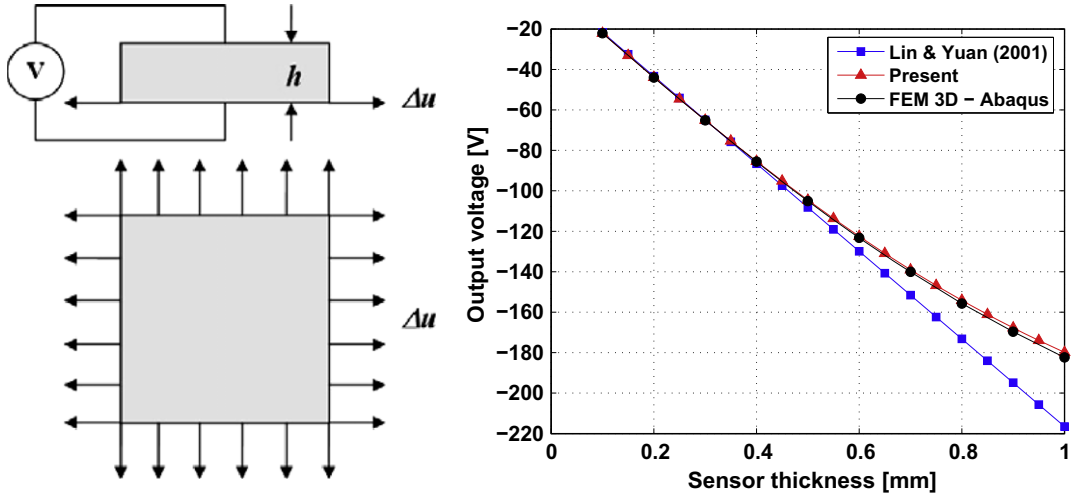

Fig. 3. Comparison between output voltages of numerical and analytical sensor for a benchmark configuration.

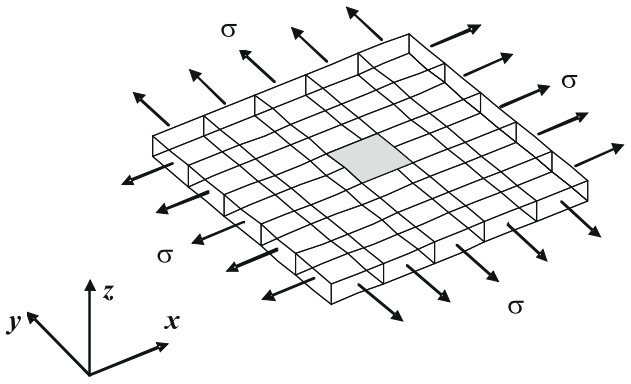

Fig. 4. Single sensor bonded on an elastic substrate and boundary element mesh.

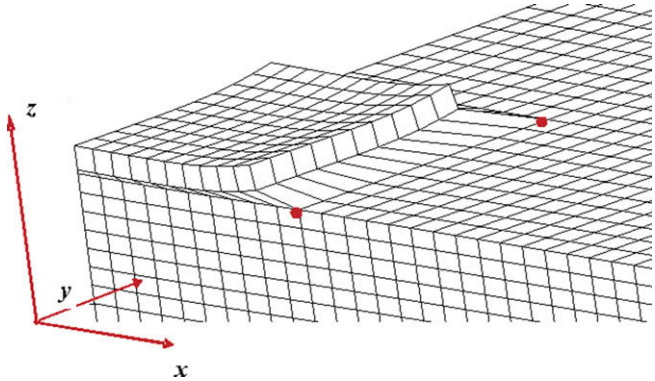

Fig. 5. FEM deformed patch detail with considered check points.

Table 2
FEM–BEM displacement comparison.

	U_x (corner)	U_y (corner)	U_x (mid)	U_y (mid)
FEM	$0.450 \cdot 10^{-3}$	$0.450 \cdot 10^{-3}$	$0.445 \cdot 10^{-3}$	$0.445 \cdot 10^{-3}$
Standard BEM	$0.447 \cdot 10^{-3}$	$0.447 \cdot 10^{-3}$	$0.444 \cdot 10^{-3}$	$0.444 \cdot 10^{-3}$
Hierarchical BEM	$0.447 \cdot 10^{-3}$	$0.447 \cdot 10^{-3}$	$0.444 \cdot 10^{-3}$	$0.444 \cdot 10^{-3}$

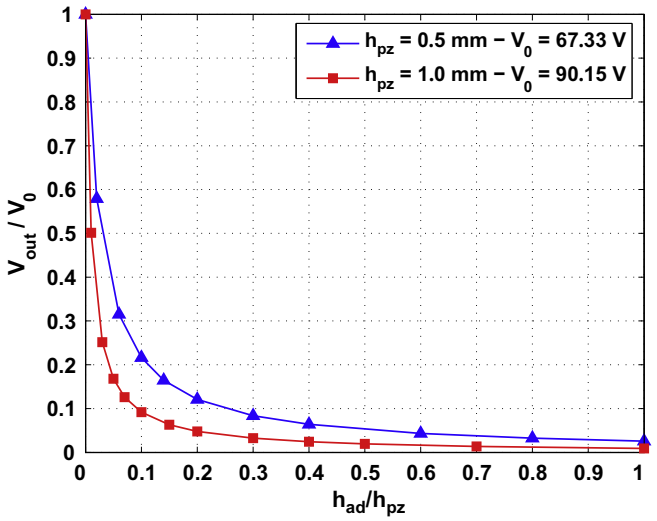

Fig. 6. Output voltage for a single sensor adhesively bonded on an elastic substrate.

The output voltage is computed for various values of the thickness h of a sensor $(10\,\text{mm} \times 10\,\text{mm} \times h)$ subjected to strains $\gamma_{11} = \gamma_{22} = 10^{-4}$ at the basis. The considered material is PZT4 and material constants are reported in Table 1.

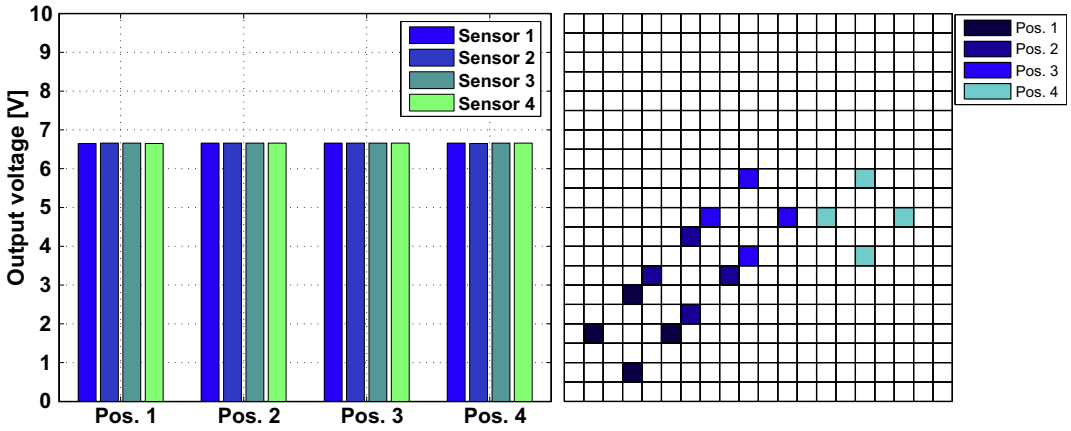

Fig. 7. Sensors response at different positions over the plate.

Table 3
Fast solver performances for the plate with four bonded sensors.

Standard assembly time (s)	259
Hierarchical assembly time (s)	190
Assembly speed up ratio	0.73
Standard solution time (s)	903
Hierarchical solution time (s)	393
Solution speed up ratio	0.44
Matrix memory storage (%)	37.36
Preconditioner memory storage (%)	10.68

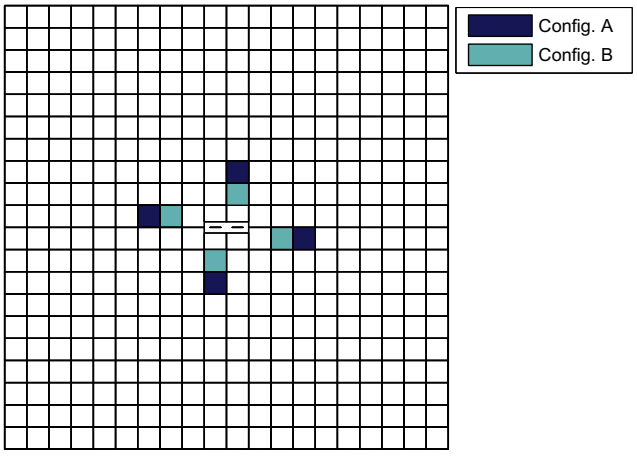

Fig. 8. Cracked plate with attached sensors.

The results are shown in Fig. 3 together with the results obtained by a full 3D FEM analysis performed with Abaqus. The computed output voltage matches very well with the analytical model for small values of h, being the simplified solution of a two-dimensional model. For higher values of the thickness, the effects of shear become more relevant and the simplified 2D model does not capture them, while the two 3D models predict the same output voltage.

After testing the electro-elastic coupling for the isolated sensor, the attachment conditions provided by Eq. (45), and then the model given by Eq. (48), are verified through comparison with finite element results. A single anisotropic patch bonded on an elastic substrate through an adhesive layer is studied. Only the mechanical behavior is considered and the electro-elastic coupling is neglected, forcing the piezoelectric constants to zero in BEM–FEM. The patch is attached on a small square aluminum plate substrate, subjected to a uniform traction acting over the four sides, as depicted in Fig. 4, which reports also the boundary element mesh used in the analysis. The patch surfaces have dimensions $(10\text{ mm} \times 10\text{ mm})$ and the patch thickness is $h_{pz} = 0.5$ mm. The substrate size is $(50\text{ mm} \times 50\text{ mm} \times 4\text{ mm})$ and it is subjected to uniform tractions $t_x = t_y = \sigma = 10.0$ MPa on the vertical sides. The elastic constants for the substrate are $E_p = 72.5$ GPa and $\nu_p = 0.33$, while for the adhesive the constants are $G = 85$ MPa and $\nu = 0.33$. A FEM detail of the 3D deformed patch is reported in Fig. 5. For comparison purposes some points at the interface between the patch-adhesive and the plate are considered. The patch corner point and the mid points, colored in red[1] in Fig. 5, are considered and the computed displacements are reported in Table 2. Very good agreement between FEM and BEM results is found.

After testing both the electro-elastic coupling for the isolated sensor and the mechanical attachment conditions for an anisotropic patch bonded on the elastic substrate, the output voltage of a piezoelectric sensor bonded on an elastic substrate is studied. The system has the same dimensions as those used for checking the attachment conditions, but now the piezoelectric constants are not forced to zero and the electro-elastic coupling is then taken into account. Moreover two different values of thickness are considered for the piezoelectric patch, $h_{pz} = 0.5$ mm and $h_{pz} = 1.0$ mm, and the adhesive layer thickness is varied between zero (no adhesive) and the thickness of the piezo-patch. The output voltage for the various adhesive thicknesses is computed and the test results are reported in Fig. 6. The diagram reports the ratio between the computed output voltage V_{out} and the output voltage V_0 obtained when no adhesive is considered for different values of the ratio between the adhesive layer thickness and the piezoelectric layer thickness. It is evident that the output voltage drops at increasing adhesive thickness, as the strain transfer from the plate to the sensor is deteriorated by the bonding layer.

After checking the single bonded sensor, a plate with a set of four piezo-patches at different locations over the plate is tested, to asses the independence of the output voltage from the sensor position, analogously to what is done in the work of Leme et al. [44]. Four different configurations are analyzed. The four single patches maintain the same relative position, but they are moved to different positions over the plate. The plate is subjected to a uniform traction along the vertical sides with $t_x = t_y = 10.0$ MPa. Test results are shown in Fig. 7. For each position sensor 1 is the one

[1] For interpretation of color in Figs. 3, 5–11, the reader is referred to the web version of this article.

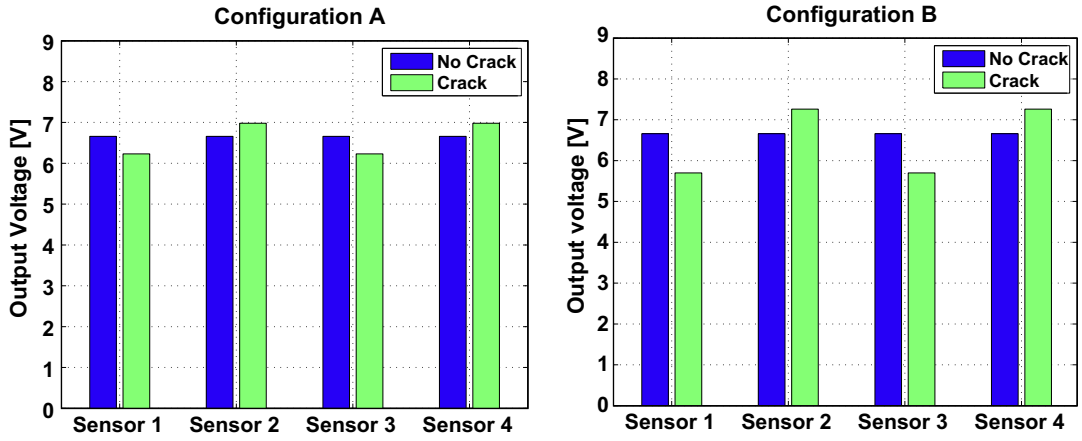

Fig. 9. Sensitivity of the sensors to the presence of cracks.

closer to the lower side of the plate shown in Fig. 7. The sensors are then counted counterclockwise. The output voltage of the set of patches does not depend on the position over the plate. It is worth noting, moreover, that the reported values resemble those reported by Leme et al. [44], who used a simple 1D sensor model.

From the computational point of view, the solution for all the considered cases has been computed by standard and hierarchical BEMs. The plate is modeled with 880 eight-node elements, corresponding to 2642 nodes. The two solution techniques give the same results in terms of output voltage, confirming the effectiveness of the solution strategy presented in Section 4.1. The hierarchical solution was computed by setting the prescribed accuracy for the collocation matrix to $\varepsilon_c = 10^{-5}$, the preconditioner accuracy to $\varepsilon_p = 10^{-2}$, the cardinality to $n_{min} = 36$, see [17] for more details. The GMRES relative accuracy was 10^{-8}. With these settings, on an Intel® Core™ 2 Duo Processor T5500 (1.66 GHz) and 2 GB of RAM, the computational performances reported in Table 3 have been obtained. The collocation matrix assembly time for both the standard and hierarchical BEMs and the solution time for both techniques are reported. Also the memory requirements for the hierarchical solver are reported in terms of percentage memory storage with respect to the full format collocation matrix.

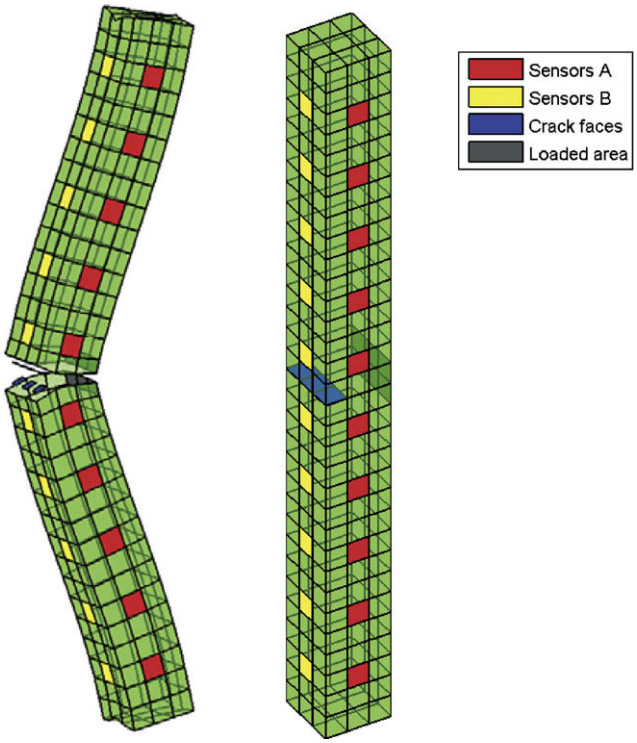

Fig. 10. Cracked beam with arrays of piezoelectric sensors.

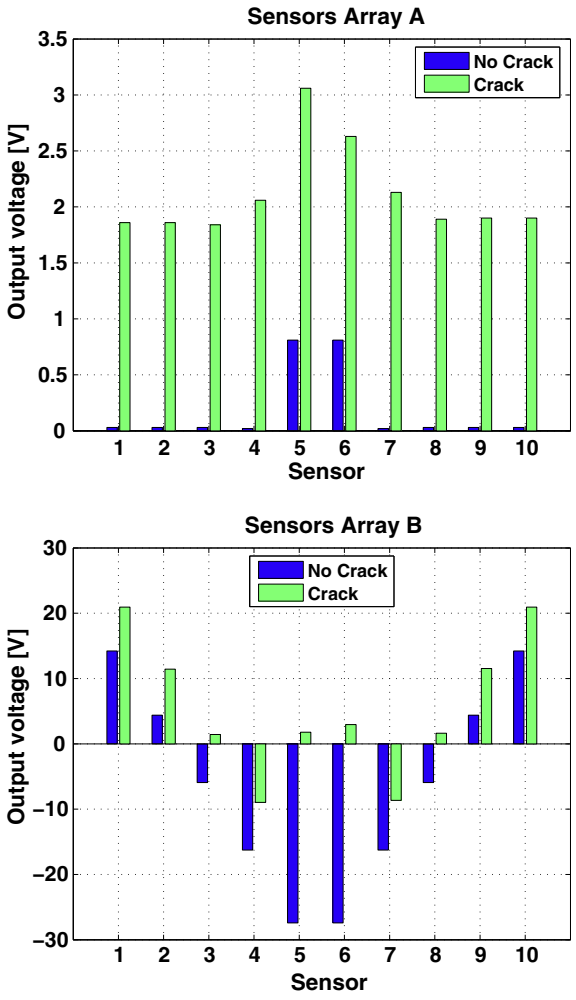

Fig. 11. Voltage output for the two beam sensor arrays.

Table 4
Computational requirements for the beam with piezo-sensors.

	No crack	Crack
Standard assembly time (s)	60	75
Hierarchical assembly time (s)	53	67
Assembly speed up ratio	0.89	0.89
Standard solution time (s)	88	104
Hierarchical solution time (s)	39	82
Solution speed up ratio	0.45	0.80
Matrix memory storage (%)	44.26	48.07
Preconditioner memory storage (%)	17.97	19.62

The sensitivity of the bonded sensors to the presence of cracks is then numerically investigated. A square 3D plate subjected to a uniform traction acting over the four vertical sides is considered. A set of four sensors is bonded on the plate. The plate sizes are 200 mm × 200 mm × 4 mm. Each sensor covers an area $S_{pz} = 1\ \text{cm}^2$ and has a thickness $h_{pz} = 0.5$ mm. The adhesive thickness is $h_{ad} = 0.125$ mm. Two different sensors configurations are considered, as illustrated in Fig. 8. The output of the sensors with and without crack is computed. The through the thickness crack has length $a = 2$ cm. The relative position between crack and sensors for the two different configurations can be inferred from Fig. 8. As it is apparent from Fig. 9, the sensor output can actually be used for structural monitoring purposes. The presence of cracks can be detected by comparing the output voltage profiles before and after the introduction of damage. An issue to be addressed is however the sensor sensitivity, since static sensors appear to be able to detect a crack when they are relatively close to it.

Finally a prismatic beam with two different arrays of piezoelectric sensors is analyzed. The beam is illustrated in Fig. 10, where both the undeformed and deformed configurations are drawn (the deformation is exaggerated for illustrative purposes). The beam transverse section is $A = 30$ mm × 30 mm and the height is $h = 32$ cm. An edge-normal crack of depth $a = 1$ cm is considered. The beam is clamped at two points at each end section and is loaded by a normal pressure $p = 15$ MPa acting over the grey elements in Fig. 10. Two different configurations for the arrays of sensors are tested separately. The output voltages from the two sensor arrays, with and without crack, are reported in Fig. 11. The sensors are counted starting from the bottom of the beam. The slight loss of symmetry in sensor output when the crack is present is due to their high sensitivity to strains, which amplifies small numerical differences in computed displacements. It can be observed that, for this kind of damage, both the sensor arrays are able to detect the presence of the crack and suggest its location. However, for configuration A, in the absence of damage, the sensors appear less loaded and this can be beneficial for their service life.

Table 4 reports time and memory requirements for the standard and hierarchical scheme. Also if the beam is not a very large-scale system, meaningful memory and time savings are achieved.

6. Conclusions

An effective model for the analysis of cracked structures with adhesively bonded piezoelectric patches has been developed. The cracked structure has been modeled using the dual boundary element method, which allows accurate analysis of crack parameters. The sensors have been modeled using a state-space finite element approach. The sensors and the host structures have been coupled naturally, expressing the sensor model in terms of interface variables and incorporating their equations in the DBEM of the underlying structure. The technique performance has been sped up using a hierarchical solver. The performed numerical experiments have shown that the sensor model offers accurate predictions of the output voltage. Medium size systems have been analyzed and the performance of the technique has been demonstrated. The proposed strategy constitutes a first step towards the modeling of SHM systems.

Appendix A. Definitions

The generalized electro-elastic quantities are defined as

$$\boldsymbol{\Gamma}_p = [\,\gamma_{11} \quad \gamma_{22} \quad \gamma_{12} \quad -E_1 \quad -E_2\,]^T, \tag{A.1}$$

$$\boldsymbol{\Sigma}_p = [\,\sigma_{11} \quad \sigma_{22} \quad \sigma_{12} \quad D_1 \quad D_2\,]^T, \tag{A.2}$$

$$\boldsymbol{\Gamma}_z = [\,\gamma_{13} \quad \gamma_{23} \quad \gamma_{33} \quad -E_3\,]^T, \tag{A.3}$$

$$\boldsymbol{\Sigma}_z = [\,\sigma_{13} \quad \sigma_{23} \quad \sigma_{33} \quad D_3\,]^T. \tag{A.4}$$

The matrix differential operators appearing in the formulation are given by

$$\mathscr{D}_\alpha = \begin{bmatrix} \partial/\partial_1 & 0 & 0 & 0 \\ 0 & \partial/\partial_2 & 0 & 0 \\ \partial/\partial_2 & \partial/\partial_1 & 0 & 0 \\ 0 & 0 & 0 & \partial/\partial_1 \\ 0 & 0 & 0 & \partial/\partial_2 \end{bmatrix}, \quad \mathscr{D}_\beta = \begin{bmatrix} 0 & 0 & \partial/\partial_1 & 0 \\ 0 & 0 & \partial/\partial_2 & 0 \\ 0 & 0 & 0 & 0 \\ 0 & 0 & 0 & 0 \end{bmatrix}. \tag{A.5}$$

The shape functions matrix appearing in Eq. (7) is defined as follows:

$$\mathbf{N}(\xi,\eta) = \begin{bmatrix} \mathbf{N}_s & \mathbf{0} & \mathbf{0} & \mathbf{0} \\ \mathbf{0} & \mathbf{N}_s & \mathbf{0} & \mathbf{0} \\ \mathbf{0} & \mathbf{0} & \mathbf{N}_s & \mathbf{0} \\ \mathbf{0} & \mathbf{0} & \mathbf{0} & \mathbf{N}_s \end{bmatrix} \tag{A.6}$$

with

$$\mathbf{N}_s(\xi,\eta) = [\,N_1 \quad N_2 \quad N_3 \quad N_4 \quad N_5 \quad N_6 \quad N_7 \quad N_8\,]. \tag{A.7}$$

In the formulation also the shape functions derivatives are used

$$\mathbf{N}_x(\xi,\eta) = \frac{\partial}{\partial x}\mathbf{N}_s(\xi,\eta), \quad \mathbf{N}_y(\xi,\eta) = \frac{\partial}{\partial y}\mathbf{N}_s(\xi,\eta). \tag{A.8}$$

Appendix B. State-space equation derivation

In this appendix some details about the derivation of the sensor equations are given. The state-space equation for piezoelectric laminates can be derived starting from the following hybrid generalized functional [18,20]:

$$\Pi = \int_\Omega \omega(\boldsymbol{\Gamma}_p, \boldsymbol{\Sigma}_z)\, d\Omega - \int_\Gamma \mathbf{T}^T(\mathbf{U} - \overline{\mathbf{U}})\, d\Gamma - \int_\Gamma \mathbf{U}^T\overline{\mathbf{T}}\, d\Gamma, \tag{B.1}$$

where

$$\omega = \boldsymbol{\Sigma}_z^T\left(\mathscr{D}_\beta + \mathbf{I}\frac{\partial}{\partial x_3}\right)\mathbf{U} + \frac{1}{2}\boldsymbol{\Gamma}_p^T\boldsymbol{\Phi}_{pp}\boldsymbol{\Gamma}_p - \frac{1}{2}\boldsymbol{\Sigma}_z^T\boldsymbol{\Phi}_{zz}\boldsymbol{\Sigma}_z + \boldsymbol{\Sigma}_z^T\boldsymbol{\Phi}_{zp}\boldsymbol{\Gamma}_p \tag{B.2}$$

and $\mathbf{T} = [\,t_1 \quad t_2 \quad t_3 \quad D_n\,]^T$ is the generalized traction vector. Overlined variables denote assigned values. The matrices appearing in Eq. (B.2) are defined as follows:

$$\mathbf{\Phi}_{zz} = \mathbf{R}_{zz}^{-1} = \begin{bmatrix} k_1 & 0 & 0 & 0 \\ 0 & k_2 & 0 & 0 \\ 0 & 0 & k_3 & k_4 \\ 0 & 0 & k_4 & k_5 \end{bmatrix}, \tag{B.3}$$

$$\mathbf{\Phi}_{zp} = \mathbf{R}_{zz}^{-1}\mathbf{R}_{zp} = \begin{bmatrix} 0 & 0 & 0 & k_6 & 0 \\ 0 & 0 & 0 & 0 & k_7 \\ k_8 & k_9 & 0 & 0 & 0 \\ k_{10} & k_{11} & 0 & 0 & 0 \end{bmatrix}, \tag{B.4}$$

$$\mathbf{\Phi}_{pp} = \mathbf{R}_{pp} - \mathbf{R}_{pz}\mathbf{R}_{zz}^{-1}\mathbf{R}_{zp} = \begin{bmatrix} k_{12} & k_{13} & 0 & 0 & 0 \\ k_{13} & k_{14} & 0 & 0 & 0 \\ 0 & 0 & k_{15} & 0 & 0 \\ 0 & 0 & 0 & k_{16} & 0 \\ 0 & 0 & 0 & 0 & k_{17} \end{bmatrix}, \tag{B.5}$$

where the constants k_i are constitutive quantities whose expressions can be obtained, after some manipulations, from Eq. (4) and correspond to the definitions given in [18].

The stationarity of the functional (B.1) with respect to $\mathbf{U}$ and $\mathbf{\Sigma}_z$, considering that $\mathbf{\Gamma}_p = \mathscr{D}_\alpha \mathbf{U}$, after applying Gauss' theorem, produces the following relationships:

$$\frac{\partial}{\partial x_3}\begin{bmatrix} \mathbf{U} \\ \mathbf{\Sigma}_z \end{bmatrix} + \begin{bmatrix} (\mathscr{D}_\beta + \mathbf{\Phi}_{zp}\mathscr{D}_\alpha) & -\mathbf{\Phi}_{zz} \\ \mathscr{D}_\alpha^T \mathbf{\Phi}_{pp}\mathscr{D}_\alpha & (\mathscr{D}_\beta^T + \mathscr{D}_\alpha^T \mathbf{\Phi}_{zp}^T) \end{bmatrix}\begin{bmatrix} \mathbf{U} \\ \mathbf{\Sigma}_z \end{bmatrix} = \begin{bmatrix} \mathbf{0} \\ \mathbf{0} \end{bmatrix} \tag{B.6}$$

and the following boundary conditions:

$$\overline{\mathbf{T}} = \overline{\mathscr{D}}_\alpha^T \mathbf{\Phi}_{pp}\mathscr{D}_\alpha \mathbf{U} + (\overline{\mathscr{D}}_\alpha^T \mathbf{\Phi}_{zp}^T + \overline{\mathscr{D}}_\beta^T + n_3\mathbf{I})\mathbf{\Sigma}_z, \tag{B.7}$$

where $\overline{\mathscr{D}}_\alpha$ and $\overline{\mathscr{D}}_\beta$ are obtained by $\mathscr{D}_\alpha$ and $\mathscr{D}_\beta$ by substituting $\partial/\partial x_i$ with n_i, which represents the ith component of the unit outward normal vector at the considered boundary point. Eqs. (B.6) and (B.7) express the piezoelectric problem in terms of state-space equation [18–20]. The matrices $\mathbf{Q}_{ij}$ in Eq. (11) are defined as follows:

$$\mathbf{Q}_{11} = \begin{bmatrix} \mathbf{0} & \mathbf{0} & -\mathbf{N}_s^T\mathbf{N}_x & -k_6\mathbf{N}_s^T\mathbf{N}_x \\ \mathbf{0} & \mathbf{0} & -\mathbf{N}_s^T\mathbf{N}_y & -k_7\mathbf{N}_s^T\mathbf{N}_y \\ -k_8\mathbf{N}_s^T\mathbf{N}_x & -k_9\mathbf{N}_s^T\mathbf{N}_y & \mathbf{0} & \mathbf{0} \\ -k_{10}\mathbf{N}_s^T\mathbf{N}_x & -k_{11}\mathbf{N}_s^T\mathbf{N}_y & \mathbf{0} & \mathbf{0} \end{bmatrix}, \tag{B.8}$$

$$\mathbf{Q}_{12} = \begin{bmatrix} k_1\mathbf{N}_s^T\mathbf{N}_s & \mathbf{0} & \mathbf{0} & \mathbf{0} \\ \mathbf{0} & k_2\mathbf{N}_s^T\mathbf{N}_s & \mathbf{0} & \mathbf{0} \\ \mathbf{0} & \mathbf{0} & k_3\mathbf{N}_s^T\mathbf{N}_s & k_4\mathbf{N}_s^T\mathbf{N}_s \\ \mathbf{0} & \mathbf{0} & k_4\mathbf{N}_s^T\mathbf{N}_s & k_5\mathbf{N}_s^T\mathbf{N}_s \end{bmatrix}, \tag{B.9}$$

$$\mathbf{Q}_{21} = \begin{bmatrix} k_{12}\mathbf{N}_x^T\mathbf{N}_x + k_{15}\mathbf{N}_y^T\mathbf{N}_y & k_{13}\mathbf{N}_x^T\mathbf{N}_y + k_{15}\mathbf{N}_y^T\mathbf{N}_x & \mathbf{0} & \mathbf{0} \\ k_{13}\mathbf{N}_y^T\mathbf{N}_x + k_{15}\mathbf{N}_x^T\mathbf{N}_y & k_{14}\mathbf{N}_x^T\mathbf{N}_x + k_{15}\mathbf{N}_y^T\mathbf{N}_y & \mathbf{0} & \mathbf{0} \\ \mathbf{0} & \mathbf{0} & \mathbf{0} & \mathbf{0} \\ \mathbf{0} & \mathbf{0} & \mathbf{0} & k_{16}\mathbf{N}_x^T\mathbf{N}_x + k_{17}\mathbf{N}_y^T\mathbf{N}_y \end{bmatrix} \tag{B.10}$$

and $\mathbf{Q}_{22} = -\mathbf{Q}_{11}^T$.

References

[1] A.K. Noor (Ed.), Structures Technology for Future Aerospace Systems, Progress in Astronautics and Aeronautics, vol. 188, American Institute of Aeronautics and Astronautics, 2000.

[2] W.C. Staszewski, C. Boller, G.R. Tomlison (Eds.), Health Monitoring of Aerospace Structures – Smart Sensor Technologies and Signal Processing, John Wiley & Sons Ltd., 2004.

[3] H. Van der Auweraer, B. Peeters, Sensors and systems for structural health monitoring, J. Struct. Control 10 (2003) 117–125.

[4] I. Chopra, Review of state of art of smart structures and integrated systems, Am. Inst. Aeronaut. Astronaut. J. 40 (11) (2002) 2145–2187.

[5] R. Ali, D.R. Mahapatra, S. Gopalakrishnan, Constrained piezoelectric thin film for sensing of subsurface cracks, Smart Mater. Struct. 14 (2005) 376–386.

[6] J. Mackerle, Sensors and actuators: finite element and boundary element analyses and simulations. A bibliography (1997–1998), Finite Elements Anal. Des. 33 (1999) 209–220.

[7] J. Zhang, B. Zhang, J. Fan, A coupled electromechanical analysis of piezoelectric layer bonded to an elastic substrate: Part I. Development of governing equations, Int. J. Solids Struct. 40 (2003) 6781–6797.

[8] R. Ali, D.R. Mahapatra, S. Gopalakrishnan, An analytical model of constrained piezoelectric thin film sensors, Sensors Actuators A 116 (2004) 424–437.

[9] G.L. Huang, C.T. Sun, The dynamic behavior of a piezoelectric actuator bonded to an anisotropic elastic medium, Int. J. Solids Struct. 43 (2006) 1291–1307.

[10] X. Lin, F.G. Yuan, Diagnostic Lamb waves in an integrated piezoelectric sensor/actuator plate: analytical and experimental studies, Smart Mater. Struct. 10 (2001) 907–913.

[11] P.S. Tua, S.T. Quek, Q. Wang, Detection of cracks in plates using piezo-actuated Lamb waves, Smart Mater. Struct. 10 (2001) 599–609.

[12] H. Fukunaga, N. Hu, F.K. Chang, Structural damage identification using piezoelectric sensors, Int. J. Solids Struct. 39 (2002) 393–418.

[13] T. Liu, M. Veidt, S. Kitipornchai, Modelling the input–output behaviour of piezoelectric structural health monitoring systems for composite plates, Smart Mater. Struct. 12 (2003) 836–844.

[14] Y.C. Liang, C. Hwu, On-line identification of holes/cracks in composite structures, Smart Mater. Struct. 13 (2004) 643–660.

[15] A. Raghavan, C.E.S. Cesnik, Finite-dimensional piezoelectric transducer modeling for guided wave based structural health monitoring, Smart Mater. Struct. 14 (2005) 1448–1461.

[16] P.S. Sumant, S.K. Maiti, Crack detection in a beam using PZT sensors, Smart Mater. Struct. 15 (2006) 695–703.

[17] I. Benedetti, M.H. Aliabadi, G. Daví, A fast 3D dual boundary element method based on hierarchical matrices, Int. J. Solids Struct. 45 (7–8) (2008) 2355–2376.

[18] G. Quing, J. Qiu, Y. Liu, A semi-analytical solution for static and dynamic analysis of plates with piezoelectric patches, Int. J. Solids Struct. 43 (2006) 1388–1403.

[19] J.S. Lee, L.Z. Jiang, Exact electroelastic analysis of piezoelectric laminae via state space approach, Int. J. Solids Struct. 33 (7) (1996) 977–990.

[20] H.Y. Sheng, J.Q. Ye, A state space finite element for laminated composite plates, Comput. Methods Appl. Mech. Engrg. 191 (2002) 4259–4276.

[21] A. Portela, M.H. Aliabadi, D.P. Rooke, The dual boundary element method: effective implementation for crack problems, Int. J. Numer. Methods Engrg. 33 (1992) 1269–1287.

[22] A. Portela, M.H. Aliabadi, D.P. Rooke, Dual boundary element incremental analysis of crack propagation, Comput. Struct. 46 (2) (1993) 237–247.

[23] Y. Mi, M.H. Aliabadi, Dual boundary element method for three-dimensional fracture mechanics analysis, Engrg. Anal. Bound. Elements 10 (1992) 161–171.

[24] Y. Mi, M.H. Aliabadi, Three-dimensional crack growth simulation using BEM, Comput. Struct. 52 (5) (1994) 871–878.

[25] M.H. Aliabadi, Boundary element formulations in fracture mechanics, Appl. Mech. Rev. 50 (2) (1997) 83–96.

[26] M.H. Aliabadi, A new generation of boundary element methods in fracture mechanics, Int. J. Fract. 86 (1–2) (1997) 91–125.

[27] A.P. Cisilino, M.H. Aliabadi, Three-dimensional BEM analysis for fatigue crack growth in welded components, Int. J. Press. Vess. Pip. 70 (1997) 135–144.

[28] A.P. Cisilino, M.H. Aliabadi, Dual boundary element assessment of three-dimensional fatigue crack growth, Engrg. Anal. Bound. Elements 28 (2004) 1157–1173.

[29] W. Hackbusch, A sparse matrix arithmetic based on *H*-matrices. Part I: Introduction to *H*-matrices, Computing 62 (1999) 89–108.

[30] W. Hackbusch, B.N. Khoromskij, A sparse *H*-matrix arithmetic. Part II: Application to multidimensional problems, Computing 64 (2000) 21–47.

[31] S. Bonn, L. Grasedyck, W. Hackbusch, Introduction to hierarchical matrices with applications, Engrg. Anal. Bound. Elements 27 (2003) 405–422.

[32] L.P.S. Barra, A.L.G.A. Coutinho, W.J. Mansur, J.F.C. Telles, Iterative solution of BEM equations by GMRES algorithm, Comput. Struct. 44 (6) (1992) 1249–1253.

[33] K. Guru Prasad, J.H. Kane, D.E. Keyes, C. Balakrishna, Preconditioned Krylov solvers for BEA, Int. J. Numer. Methods Engrg. 37 (1994) 1651–1672.

[34] C.Y. Leung, S.P. Walker, Iterative solution of large three-dimensional BEM elastostatic analyses using the GMRES technique, Int. J. Numer. Methods Engrg. 40 (1997) 2227–2236.

[35] M. Merkel, V. Bulgakov, R. Bialecki, G. Kuhn, Iterative solution of large-scale 3D-BEM industrial problems, Engrg. Anal. Bound. Elements 22 (1998) 183–197.

[36] E.E. Tyrtyshnikov, Mosaic-skeleton approximations, Calcolo 33 (1996) 47–57.

[37] S.A. Goreinov, E.E. Tyrtyshnikov, N.L. Zamarashkin, A theory of pseudoskeleton approximations, Linear Algebra Appl. 261 (1997) 1–21.

[38] M. Bebendorf, Approximation of boundary element matrices, Numer. Math. 86 (2000) 565–589.

[39] M. Bebendorf, S. Rjasanow, Adaptive low-rank approximation of collocation matrices, Computing 70 (2003) 1–24.
[40] M. Bebendorf, R. Grzhibovskis, Accelerating Galerkin BEM for linear elasticity using adaptive cross approximation, Math. Methods Appl. Sci. 29 (2006) 1721–1747.
[41] Y. Saad, M.H. Schultz, GMRES: a generalized minimal residual algorithm for solving nonsymmetric linear systems, SIAM J. Sci. Stat. Comput. 7 (3) (1986) 856–869.
[42] M. Bebendorf, Hierarchical LU decomposition-based preconditioners for BEM, Computing 74 (2005) 225–247.
[43] L. Grasedyck, Adaptive recompression of *H*-matrices for BEM, Computing 74 (2005) 205–223.
[44] S.P.L. Leme, M.H. Aliabadi, L.M. Bezerra, P.W. Partridge, An investigation into active strain transfer analysis in piezoceramic sensor system for structural health monitoring using the dual boundary element method, Struct. Durabil. Health Monitor. 3 (3) (2007) 121–132.